www.papersinphysics.org

Received: 27 February 2026, Accepted: 22 June 2026
Edited by: Oscar Martínez, Universidad de Buenos Aires, Argentina
Licence: Creative Commons Attribution 4.0
DOI: https://doi.org/10.4279/PIP.180004

ISSN 1852-4249

Power flux in a three-layer slab waveguide with graphene interfaces and a metamaterial core

Nawal N. Amsir,[1] Hassan A. Yasser,[2] *

This paper presents a theoretical study of the electromagnetic wave propagation in a three-layer slab waveguide with a metamaterial core and graphene interfaces on each end. The dispersion relation, field distribution, and power-flux expressions are then analytically formulated to obtain the impact of the magnetic permeability of the central layer and graphene Fermi energy on the guided modes. It is found that by changing core permeability, the basic TE_0 mode can be suppressed or allowed, and other higher-order modes can propagate consistently. The analysis of power flux shows how there is forward and backward energy flow, where negative values of the flux show that there is backwards-wave flow in the structure. Moreover, mode confinement and alteration in power distribution within the layers occur with an increase in Fermi energy. It is seen that graphene-metamaterial waveguides have a bright future in terms of reconfigurable photonic platforms, with potential uses in optical communication, slow-light devices, and plasmonic control technologies.

1 Introduction

Terahertz technology and the rapid development in the field of photonic engineering have further amplified the need to develop more complex waveguide designs that could allow a high level of control of the electromagnetic field[1]. Metamaterials have received considerable interest in these platforms due to their ability to exhibit unusual electromagnetic behaviors like negative permittivity, negative permeability, and near-zero refractive index. The materials that have been engineered allow novel wave effects, such as backwards-wave propagation, slow-light behavior, sub-wavelength confinement, and enhanced field localization effects, which are hard to accomplish with more conventional dielectric media. As a result, waveguides based on metamaterials have become a promising basis for compact high-performance optical components[2–4]. Simultaneously, graphene has become a tunable two-dimensional material that possesses an outstanding electrical conductivity, a high level of light-matter interaction, and high dynamical control due to the ability to adjust the Fermi level[5]. Graphene, unlike conventional metals, is able to allow intraband and interband transitions, which allow active control of the surface conductivity of the material through chemical doping or applied bias[6]. This tunability offers a strong tool for management of dispersion properties, mode control and energy transport in photonic structures. This has created a hybrid platform between negative-index capabilities and electro-optical reconfigurability because of the integration of graphene with metamaterials, which are highly applicable to waveguides, modulators, sensors, and terahertz devices[7].

Some studies have been conducted in recent years on waveguides that use metamaterials or graphene to raise the confinement of electromagnetism and tunability. As an example, Jablan et al. have shown the tunable plasmonic response of graphene-based structures and mention that they can be used in active photonic control[8], whereas Razzaza et al. examined graphene-loaded

* hassan.yasser@sci.utq.edu.iq

[1] Ministry of Education, Directorate of Education in Thi-Qar, Iraq.

[2] Thi-Qar University, Science College, Physics Department, Iraq.

waveguides in the environment of magnetic materials and have verified that modulating the Fermi level has a significant impact on guided-mode behavior[9]. On the same note, Heidari and Ahmadi presented graphene-metamaterial waveguides, which can support the propagation of line-waves with high reconfigurability[10], whereas Zhang et al. found that graphene-metamaterial waveguides can manipulate TE/TM modes and realize dispersion tuning[11]. As much as the studies are of benefit, they are more inclined towards the dispersion properties or mode-control mechanisms rather than the power-flux behavior, forward/backwards-wave identification, and the combined effect of the variation of permeability and the control of graphene Fermi energy.

In this paper, a single theoretical framework which explores the dispersion properties and the energy-flux behavior of a three-layer slab waveguide with a metamaterial core and with graphene interfaces is presented. The field distribution, dispersion relation and power-flux expression formulations are formulated analytically, allowing the accurate determination of the effect of Fermi energy and magnetic permeability on mode propagation. The findings indicate tunable forward-to-backwards guided mode transitions, such as fundamental TE_0 mode suppression or activation in certain conditions. This gives further physical insight into tunability effects in metamaterial-graphene waveguides and offers a firm basis for how to design reconfigurable photonic systems to apply to future optical communication, sensing systems, and devices based on graphene and terahertz.

2 Graphene conductivity

Optical conductivity of the graphene is a basic parameter in the plasmonic properties of graphene, and it greatly affects the electromagnetic wave propagation at the graphene-based waveguides. In contrast with Drude's description of plasmons of typical metals, the graphene system not only possesses the linear band structure around the Dirac point but also enables intraband as well as interband electronic transitions. Thus, its dynamically modulated complex surface conductivity can be achieved through the application of external bias, temperature variation or chemical doping. It is an adjustable feature that renders graphene an excellent platform for reconfigurable photonic and plasmonic structures. The dynamic conductivity of a graphene sheet can be expressed using the Kubo formula in terms of the intraband contribution and the interband contribution as[12, 13]

$$\sigma(\omega) = \sigma_{intra}(\omega) + \sigma_{inter}(\omega), \tag{1}$$

where $\sigma_{intra}(\omega)$ and $\sigma_{inter}(\omega)$ represent the intraband and interband contributions, respectively:

$$\sigma_{intra} = -i\frac{e^2 k_B T}{\pi\hbar^2(\omega - 2i\Gamma)} \times \left[\frac{\mu_c}{k_B T} + 2\ln\left(1 + e^{-\mu_c/k_B T}\right)\right] \tag{2a}$$

$$\sigma_{inter} = -\frac{ie^2}{4\pi\hbar}\ln\left[\frac{2|\mu_c| - (\omega - 2i\Gamma)\hbar}{2|\mu_c| + (\omega - 2i\Gamma)\hbar}\right] \tag{2b}$$

where Γ is a phenomenological scattering rate that is assumed to be independent of energy, carrier energy, and is related to the relaxation time τ by $\Gamma = 1/2\tau$. μ_c is the chemical potential that is approximately equal to the Fermi energy E_F for $E_F \gg k_B T$, T is the temperature, e is the electron charge, k_B is the Boltzmann constant, and $\hbar$ the reduced Planck constant.

The intraband portion dominates at low energies of photons (THz-mid-IR range) and leads to plasmon excitation in doped graphene. At room temperature, the intraband term reduces to an expression similar to the classical Drude response for $E_F \gg k_B T$. As E_F rises, intraband conductivity increases, as does plasmon confinement, with diminished loss, a paramount trait utilized in actively tunable plasmonic devices[14]. The interband term becomes relevant at high photon energies when electrons can be excited from valence to conduction band, i.e., interband transitions induce absorption peaks and attenuate plasmons at optical frequencies.

When $\hbar\omega < 2E_F$, Pauli blocking kills interband absorption, with a consequent increase in the imaginary part of the conductivity and much stronger plasmon resonance. When $\hbar\omega > 2E_F$ interband transitions increase, and the conductivity turns more to a real value, i.e., a larger dissipation. The real part of the conductivity refers to energy absorption (loss)[15]. The imaginary part determines plasmon confinement and phase response. Plasmon frequency is shifted to a higher frequency with increasing Fermi energy level, due to better confinement and easier tuning. The ratio $\sigma_{intra}/\sigma_{inter}$ controls the operating frequency region. By controlling the conductivity behavior, it is possible to achieve accurate design of graphene-based plasmonic waveguides, modulators, and tunable photonic devices[16].

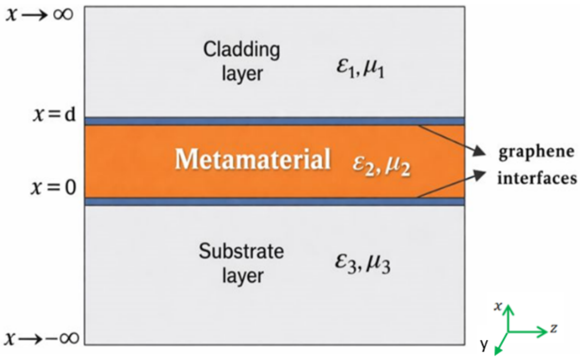

Figure 1: An asymmetric three-layer slab waveguide with graphene interfaces, where the central layer is a metamaterial.

3 Three-layer slab waveguide with metamaterials

A planar waveguide is characterized by parallel boundaries in one direction (x-axis), but is infinite in extent in the lateral directions (y-axis and z-axis). In this work, we investigate an asymmetric slab waveguide structure sketched in Fig. 1.

A core slab layer with permeability and permittivity (μ_2, ϵ_2) occupying the region $0 < x < d$ is sandwiched between a substrate with permeability and permittivity (μ_3, ϵ_3) occupying the region $-\infty < x < 0$ and a cover cladding with permeability and permittivity (μ_1, ϵ_1) occupying the region $d < x < \infty$. Their structure is uniform in the y- and z-directions. Only a two-dimensional problem $\partial/\partial y = 0$ is considered because the index profile is independent of the y-direction. For this waveguide type, the modes are either TE or TM. Electromagnetic waves can be expressed as a linear combination of TE and TM modes. The model treats the graphene layer as infinitely thin. This modeling approach is accurate if the graphene thickness, approximately 0.34 nm, is much less than the wavelength of the electromagnetic waves presents in the system. In the terahertz to mid-infrared frequency ranges, the wavelengths are in the order of several micrometers, which is several orders of magnitude larger than the thickness of the graphene. Under these conditions, graphene can be represented as an infinitely thin 2D conductor. This approach is common in theoretical and computational modeling of graphene waveguides and plasmonic devices.

4 Wave equation and energy flux

The general dispersion theory of multilayer waveguides has been extensively studied in classical[17] and modern works[18], while the present study focuses on graphene-metamaterial configurations. All the analyses of electromagnetic wave propagation depend on Maxwell's equations that govern the time dependence of the intensity of the electric and magnetic fields. We can also introduce the electric permittivity and the magnetic permeability to characterize the response of the materials to external electric and magnetic fields. The result will be[19]

$$\vec{\nabla} \times \vec{E} = -\mu \frac{\partial \vec{H}}{\partial t} \tag{3a}$$

$$\vec{\nabla} \times \vec{H} = \epsilon \frac{\partial \vec{E}}{\partial t} \tag{3b}$$

where $\vec{E}$ is the electric field and $\vec{B}$ is the magnetic flux density. The electric and magnetic fields for the TE waves propagating along the z-axis with angular frequency w and wavenumber β_z can be expressed as[20]:

$$\vec{E} = \begin{bmatrix} 0 \\ E_y \\ 0 \end{bmatrix} e^{i(\beta_z z - wt)}, \quad \vec{H} = \begin{bmatrix} H_x \\ 0 \\ H_z \end{bmatrix} e^{i(\beta_z z - wt)}. \tag{4}$$

For similar parameters, the electric and magnetic fields of TM waves propagating along the z-axis will be:

$$\vec{E} = \begin{bmatrix} E_x \\ 0 \\ E_z \end{bmatrix} e^{i(\beta_z z - wt)}, \quad \vec{H} = \begin{bmatrix} 0 \\ H_y \\ 0 \end{bmatrix} e^{i(\beta_z z - wt)}. \tag{5}$$

Substituting Eq. (4) in Eq. (3) and simplifying the result yields

$$E_x = \frac{\beta_z}{\varepsilon w} H_y, \; E_y = \frac{i}{\varepsilon w}\left(\frac{\partial H_x}{\partial z} - \frac{\partial H_z}{\partial x}\right), \; E_z = \frac{i}{\varepsilon w}\frac{\partial H_y}{\partial x}, \tag{6a}$$

$$H_x = -\frac{\beta_z}{\mu w} E_y, \; H_y = \frac{-i}{\mu w}\left(\frac{\partial E_x}{\partial z} - \frac{\partial E_z}{\partial x}\right), \; H_z = \frac{-i}{\mu w}\frac{\partial E_y}{\partial x}. \tag{6b}$$

Using Eqs. (6a) and (6b) and the fact $\partial E_y/\partial z = i\beta_z E_y$, simplifying the result and rearranging the final equation, we get the wave equation in the central layer:

$$\frac{\partial^2 E_y}{\partial x^2} + k_o^2(\epsilon_2\mu_2 - n_{\mathtt{eff}}^2)E_y = 0, \tag{7}$$

where $\beta_z = k_o n_{\mathtt{eff}}$ is the propagation constant along the longitudinal direction, $n_{\mathtt{eff}}$ is the modal index of the propagation mode, and $\epsilon_2 = \epsilon/\epsilon_o$ and $\mu_2 = \mu/\mu_o$ are the relative permittivity and permeability of the central layer. The free space wavenumber is defined as $k_o = w/c$. Consequently, Eqs. (6a) and (6b) will be used to explain the other components of the electric and magnetic fields. The solutions of Eq. (7) in the three layers are given by

$$E_{y3} = Ae^{-k_3(x-d)} \quad x \geq d, \tag{8a}$$
$$E_{y2} = Be^{-ik_2 x} + Ce^{ik_2 x} \quad 0 \leq x \leq d, \tag{8b}$$
$$E_{y1} = De^{k_1 x} \quad 0 \geq x, \tag{8c}$$

where $k_3 = k_o\sqrt{n_{\texttt{eff}}^2 - \epsilon_3\mu_3}$, $k_1 = k_o\sqrt{n_{\texttt{eff}}^2 - \epsilon_1\mu_1}$, $k_2 = k_o\sqrt{\epsilon_2\mu_2 - n_{\texttt{eff}}^2}$. The parameters A, B, C, D represent the amplitudes of the waves in the different layers. The parameters k_j ($j = 1, 2, 3$) represent the propagation constants in the x-direction for the three layers.

The magnetic field component H_z can be calculated using Eq. (6b) and Eq. (8), then matching the components of the tangential electric fields: $E_{y1} = E_{y2}$ at $x = 0$ and $E_{y3} = E_{y2}$ at $x = d$, and the magnetic fields $H_{z1} - H_{z2} = \sigma E_{y1}$ at $x = 0$ and $H_{z2} - H_{z3} = \sigma E_{y2}$ at $x = d$, yielding

$$A - Be^{-ik_2 d} - Ce^{ik_2 d} = 0, \tag{9a}$$
$$B + C - D = 0, \tag{9b}$$
$$r_1 A - Be^{-ik_2 d} + Ce^{ik_2 d} = 0, \tag{9c}$$
$$r_2 B + r_3 C - iD = 0, \tag{9d}$$

where

$$r_1 = \frac{\mu_o\mu_2}{k_2}\left(\sigma w - \frac{ik_3}{\mu_o\mu_3}\right), \tag{10a}$$
$$r_2 = \frac{\mu_o\mu_1}{k_1}\left(\sigma w + \frac{k_2}{\mu_o\mu_2}\right), \tag{10b}$$
$$r_3 = \frac{\mu_o\mu_1}{k_1}\left(\sigma w - \frac{k_2}{\mu_o\mu_2}\right). \tag{10c}$$

The system in Eq. (9) has a nontrivial solution only if the determinant of the coefficients is zero. This determinant is

$$\tan(k_2 d) = i\frac{r_3(1-r_1) + r_2(1+r_1) - 2i}{r_2(1+r_1) - r_3(1-r_1) - 2ir_1}. \tag{11}$$

Using the above definitions of r_1, Eq. (11) will be reduced to the following formulas:

$$k_2 d = \tan^{-1} W_1 + \tan^{-1} W_2 + n\pi, \quad n = 0, 1, 2, ..., \tag{12}$$

where

$$W_1 = \frac{k_1\mu_2}{\mu_1 k_2} + i\sigma w\mu_0\frac{\mu_2}{k_2}, \tag{13a}$$
$$W_2 = \frac{k_3\mu_2}{\mu_3 k_2} + i\sigma w\mu_0\frac{\mu_2}{k_2}. \tag{13b}$$

This equation is called the characteristic equation of TE modes. This equation will be solved numerically by the graphics method to determine the ordered pair $(w, n_{\texttt{eff}})$ that satisfies both sides of the equation. These ordered pairs, which satisfy the characteristic equation, are later used to determine the distribution of fields, powers, and other variables according to the chosen mode. Under certain conditions, the equation can be solved for all values of n (which represents the mode order), but it is not necessary to obtain the solution for all values of n, which means that this mode does not appear. Depending on the result in Eq. (12), the constants in the system in Eq. (9) may be determined, and the fields will be:

$$E_{y3} = e^{-k_3(x-d)} \quad x \geq d, \tag{14a}$$
$$E_{y2} = \frac{(1+r_1)e^{-ik_2(x-d)} + (1-r_1)e^{ik_2(x-d)}}{2[\cos k_2 d + ir_1 \sin k_2 d]} \quad \text{for } 0 \leq x \leq d, \tag{14b}$$
$$E_{y1} = \frac{1}{\cos k_2 d + ir_1 \sin k_2 d}e^{k_1 x} \quad 0 \geq x. \tag{14c}$$

The characteristic equation and magnetic fields of TM modes can be obtained by replacing each permeability with the corresponding permittivity. We will focus only on the TE modes, since the TM type differs slightly from them. Ideally, all modes of propagation can be investigated, but currently only TE modes of propagation will be analyzed. TE modes of propagation are justified as a physical phenomenon since TE modes of propagation are influenced the most by the refractive-index gradient of the waveguide core. Therefore, in terms of a graded refractive-index profile, the core profile determines the TE modes confinement and dispersion characteristics the most. On the other hand, the TM modes possess a longitudinal electric-field component that strongly interacts with the surface conductivity of the graphene layers and interfaces. This contact creates a plasmonic effect less influenced by the refractive-index gradient present at the core of the layer. This means the graded refractive-index profile has a minimal effect on TM modes. Because of this, analyzing only TE modes adequately describes the waveguide structure's modal behavior.

Energy flux in the waveguide is considered an essential parameter, which may be calculated using the Poynting vector averaged over the period T, and it is defined as $\vec{S} = Re\{\vec{E} \times \vec{H}\}/2$. For a monochromatic plane wave where the energy flux is directed along the z-axis, the transverse profile S_z of guided modes for given waveguide parameters can be constructed as $S_z = \beta_z|E|^2/2\mu w$. The power flux can be obtained as an integral of the Poynting vector. That is, the energy flux per unit length for TE mode is given by[21]:

$$\begin{aligned} P_{tot}^{TE} &= \frac{\beta_z}{2w\mu_3}\int_{-\infty}^{0}|E_{y3}|^2dx + \frac{\beta_z}{2w\mu_2}\int_{0}^{d}|E_{y2}|^2dx \\ &+ \frac{\beta_z}{2w\mu_1}\int_{d}^{\infty}|E_{y1}|^2dx \\ &= P_3^{TE} + P_2^{TE} + P_1^{TE}. \end{aligned} \tag{15}$$

Substituting Eq. (14) into Eq. (15), performing integrations, ordering and rearranging, the powers in each layer will be:

$$P_1^{TE} = \frac{\beta_z|A|^2}{4w\mu_o k_1\mu_1}, \tag{16a}$$

$$P_2^{TE} = \frac{\beta_z|A|^2}{4w\mu_o\mu_2 k_2}Q, \tag{16b}$$

$$P_3^{TE} = \frac{\beta_z|A|^2}{4w\mu_o k_3\mu_3}, \tag{16c}$$

where

$$\begin{aligned} Q &= (1+|r_1|^2)k_2d \\ &- \sin k_2d[(1-|r_1|^2)\cos k_2d + 2Im(r_1)\sin k_2d]. \end{aligned} \tag{17}$$

We can now emphasize the following important issue: for any specified value of waveguide parameters, the powers in the cladding and substrate layers are always positive. For TE modes, to investigate the net power flux in the waveguide, we used the normalized power that can be expressed as[19]

$$\overline{P}^{TE} = \frac{P_1^{TE} + P_2^{TE} + P_3^{TE}}{|P_1^{TE}| + |P_2^{TE}| + |P_3^{TE}|}. \tag{18}$$

When $\overline{P}^{TE} < 0$, the net power flow of the guided mode is antiparallel with the direction of phase flow, and this wave is called the backward wave. The opposite result can occur when $\overline{P}^{TE} > 0$ and this wave is called the forward wave. When we deal with electrical modes, only magnetic permeability will appear in the relationship of dispersion, fields, and power. Therefore, when we discuss the idea of metamaterials and say that we will make magnetic permeability negative, this implicitly means that we will make electrical permittivity negative, even if we do not explicitly state this.

Table 1: Simulation parameters for the three-layer slab waveguide.

Parameter	Value	Parameter	Value
$\mu_1 = \mu_3$	1.1	μ_o	$4\pi \times 10^{-7}$ (H/m)
$\epsilon_1 = \epsilon_3$	1.3	v_F	1×10^6 (m/s)
μ_2	1.5	μ	1×10^4 (cm^2/Vs)

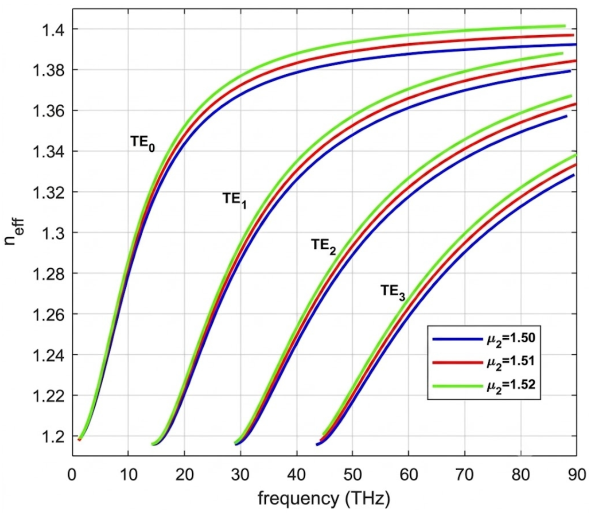

Figure 2: Dispersion relation using a conventional material central layer at different positive values of μ_2 at $E_F = 0$, showing an upward shift with higher permeability values.

5 Results and discussion

The numerical values gathered in Table 1 are used for the simulations, and any subsequent modification to these base parameters will be explicitly noted and justified. For all the evaluations, we set $\mu_1 = \mu_3$ and $\epsilon_1 = \epsilon_3$ to treat the waveguide structure as symmetric. The characteristic relaxation time is defined as $\tau = \mu E_F/(ev_F^2)$, where μ denotes the carrier mobility and v_F is the Fermi velocity in graphene. Before analyzing the dispersion curves of the TE modes, it is

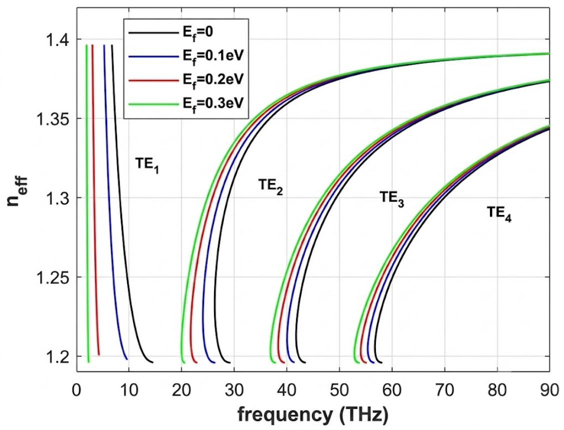

Figure 3: Dispersion curves showing the effective refractive index for guided modes under a metamaterial core layer ($\mu_2 = -1.5$) at various Fermi energies.

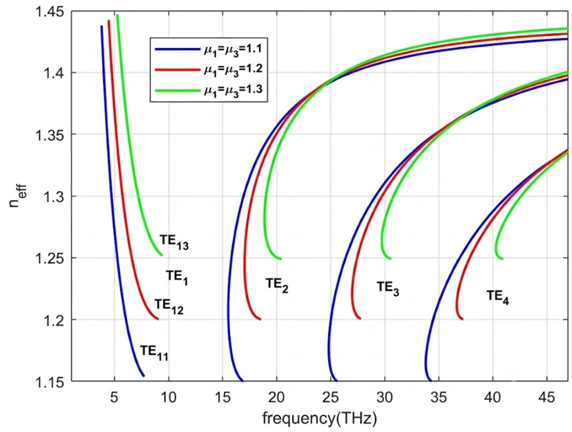

Figure 4: Dispersion relation curves for guided modes exhibiting slow light features immediately above the cutoff frequencies for different cladding permeabilities at $\mu_2 = -1.6$.

useful to clarify the physical meaning of the index n in the TE_n notation. The mode order n corresponds to the exact number of half-wave variations of the transverse electric field components along the waveguide core. Consequently, the fundamental mode TE_0 has exactly one field intensity peak and does not possess any zero-crossings, whereas higher-order modes like TE_1, TE_2, and so on, exhibit nodes and zero-crossings. It is critical to mention that not all waveguides support the fundamental TE_0 mode, particularly when dealing with metamaterial core layers, since its existence depends significantly on the core thickness d, among other electromagnetic boundary parameters.

Fig. 2 shows the dispersion relation calculated for a conventional material core layer at different positive values of core magnetic permeability μ_2 under unprimed intrinsic graphene conditions ($E_F = 0$). The line colors blue, red, and green map to $\mu_2 = 1.50$, 1.51, and 1.52, respectively. As the frequency grows, the effective refractive index $n_{\mathtt{eff}}$ for each mode increases and tends to saturate at higher frequencies. At lower frequencies, the modal effective refractive index starts from a clear cutoff value and grows non-linearly with frequency. For each individual TE mode, as μ_2 is raised from 1.50 to 1.52, the dispersion branches shift slightly upwards. This indicates that the effective refractive index increases along with μ_2. The visible separation between the curves for different core permeabilities at a given operating frequency suggests that higher core permeabilities yield larger effective refractive indices.

The behavior changes dramatically when substituting the dielectric core with a metamaterial central layer characterized by a negative magnetic permeability ($\mu_2 = -1.5$). Figure 3 highlights the dispersion curves under these conditions for different graphene Fermi levels, where the black, blue, red, and green lines stand for $E_F = 0$, 0.1, 0.2, and 0.3 eV, respectively. These modes possess clear cut-off frequencies beyond which propagation is permitted, as expected for TE modes in planar guides. As the transverse mode order increases from TE_1 to TE_4, the corresponding cut-off frequency also shifts upward, which is typical of higher-order modes. The negative permeability within the central metamaterial core prompts unusual dispersion features that support backwards-wave propagation or slow-light behavior. This is physically evidenced by the slight leftward bending of the curves at their origin, most visibly in the higher-order modes TE_2, TE_3, and TE_4. The negative μ_2 parameter establishes a negative phase velocity regime, significantly altering the dispersion topology compared to conventional structures. As E_F increases, the effective index increases at a given frequency. This stems from the rise in graphene's surface conductivity, which strengthens the confinement of the electromagnetic wave within the metamaterial slab. Higher E_F values produce greater optical confinement and more stable waveguiding, creating larger values of $n_{\mathtt{eff}}$. Even though $n_{\mathtt{eff}}$ remains positive within these regions, the negative slope reveals a reverse-propagation regime at the beginnings of the curves.

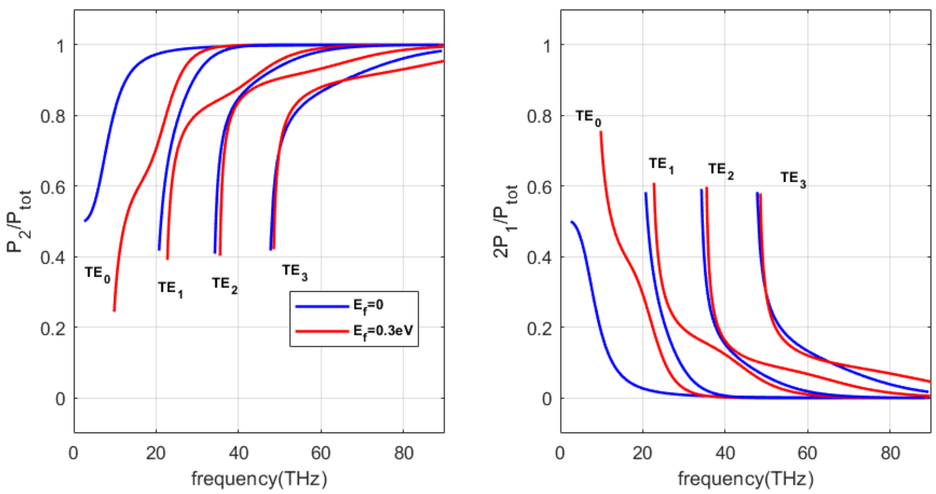

Figure 5: Normalized power distribution P_2/P_{tot} and $2P_1/P_{tot}$ for intrinsic and biased graphene states with a conventional core layer ($\mu_2 = 1.6$).

The influence of changing the surrounding cladding permeability ($\mu_1 = \mu_3$) for a metamaterial core ($\mu_2 = -1.5$) at $E_F = 0$ is depicted in Fig. 4. The blue, red, and green curves represent $\mu_1 = 1.1$, 1.2, and 1.3, respectively. Decreasing the surrounding medium permeability shifts the cut-off points to lower values, implying that a lower cladding permeability supports modes at lower frequencies. This phenomenon occurs because increasing the magnetic permeability elevates the wave impedance of the guiding layer, altering the mode confinement and phase-matching conditions at the interfaces. The shift is more pronounced for higher-order modes like TE_3 and TE_4 due to their stronger dependence on the total optical path length and field penetration into the cladding.

It is important to notice in both Fig. 3 and Fig. 4 that each mode starts at its cut-off frequency with an abrupt, near-vertical jump where $n_{\texttt{eff}}$ increases rapidly as a function of frequency before asymptotically approaching a flat line. This steep vertical slope is the main feature associated with the slow-light phenomenon. When the effective refractive index varies exceptionally fast with frequency, the light traveling in that mode experiences a much larger effective group index than its raw phase index value would suggest. A high group index corresponds to a significantly lower group velocity, meaning that the optical energy is transported along the waveguide at a much lower speed. This is exactly what takes place at the cut-off region of each TE mode: the narrow frequency span where the curve is steep represents the slow-light region. As the frequency moves away from cut-off, the curve flattens out, $dn_{\texttt{eff}}/df$ decreases, and the wave returns to standard propagation speeds. In Fig. 3, tuning E_F shifts this slow-light region along the THz spectrum, demonstrating electrical reconfigurability. Similarly, Fig. 4 shows that varying the cladding permeability deforms this steep portion, providing an extra tool to customize at which frequency slow light is achieved.

Additionally, the analysis of Figs. 2 to 4 proves that field confinement at low frequencies is weak, and the modal index matches that of the outer claddings. Stronger coupling between the electromagnetic wave and the metamaterial core localizes the fields at higher frequencies, triggering the rise of $n_{\texttt{eff}}$ toward saturation. The upward movement of the curves with higher E_F is justified by the increased surface conductivity of graphene, which lowers plasmonic dissipation and improves mode confinement. The suppression or attenuation of higher-order TE modes occurs when the phase-matching condition between the core and claddings is no longer satisfied, meaning that the wave can no longer be confined as a bounded standing wave inside the core region.

The analysis of energy transport is carried out through the normalized power distribution. Figure 5 shows the normalized power spectrum versus frequency for the first four TE modes (TE_0 to TE_3, corresponding to $n = 0$ to 3) using a conventional core material layer ($\mu_2 = 1.6$). The plots evaluate the fractional power

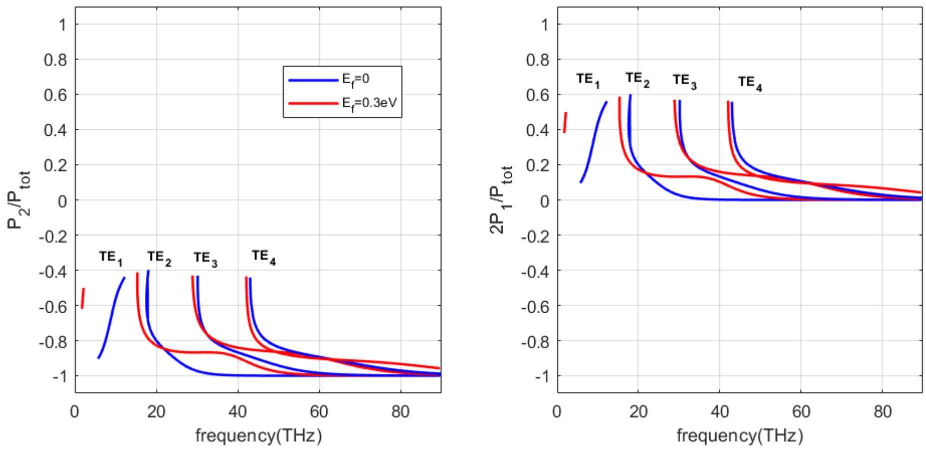

Figure 6: Normalized power as a function of frequency for the first four TE modes ($TE_1 - TE_4$) for the metamaterial central layer ($\mu_2 = -1.6$).

inside the core (P_2/P_{tot}) and the power distributed in the surrounding claddings ($2P_1/P_{tot}$) under two specific states: intrinsic graphene at $E_F = 0$ (blue curves) and biased graphene at $E_F = 0.3$ eV (red curves). At lower frequencies, the guide operates in a weakly guiding regime, and most of the electromagnetic energy is carried within the claddings, as shown by the high starting values of $2P_1/P_{tot}$. As the frequency increases, a clear transition takes place: the modes become tightly localized in the core layer, forcing $P_2/P_{tot} \approx 1$ asymptotically while the cladding power drops to zero. This transition frequency moves to higher values as the mode order n grows. Shifting E_F to 0.3 eV adjusts the surface conductivity of the graphene interfaces, modifying the interaction between the core and the guided waves. For the fundamental TE_0 mode, raising the Fermi level shifts the transition region to a higher frequency. In contrast, for the higher-order modes (TE_1, TE_2, TE_3), the transition toward core confinement occurs at lower frequencies in the biased case than in the intrinsic case. Remarkably, at high frequencies, the fundamental TE_0 mode at $E_F = 0.3$ eV experiences a small reduction in core power saturation, indicating that some energy leaks back into the claddings at the high end of the band.

Fig. 6 displays the resulting normalized power as a function of frequency for the first four TE modes (TE_1 to TE_4) when using the metamaterial central layer ($\mu_2 = -1.6$). The graph examines the fractional power in the core P_2/P_{tot} and the cladding $2P_1/P_{tot}$ at $E_F = 0$ (blue lines) and $E_F = 0.3$ eV (red lines). Near the cut-off frequencies, a large portion of the total power flows through the claddings. As the frequency increases, the modes become strongly guided, and P_2/P_{tot} converges toward unity while $2P_1/P_{tot}$ drops to zero. This transition shifts to higher frequencies for higher mode numbers. Introducing a non-zero Fermi level ($E_F = 0.3$ eV) serves as an effective mechanism to control the confinement. For the higher-order modes TE_2 to TE_4, the transition to core confinement in the biased state happens at lower frequencies than in the intrinsic state, meaning that doping the graphene interface enhances the wave-core interaction, producing tightly confined modes at lower cutoffs. Interestingly, the TE_1 mode exhibits a crossover effect, where the biased state initially requires a slightly larger frequency to achieve the same confinement. Additionally, the biased curves for TE_3 and TE_4 show a minor departure from perfect saturation at high frequencies, representing a small energy redistribution.

To inspect the mode conversion mechanism across the graphene sheets, Fig. 7 depicts the normalized power carried by the core layer (P_2) and the outer layers ($2P_1$) of an all-dielectric three-layer structure for mode orders $n = 0, 1, 2,$ and 3. The black and red curves stand for the intrinsic graphene case ($E_F = 0$ eV), while the blue and green curves show the doped graphene state ($E_F = 0.3$ eV). For each mode order n, the two power components are perfectly complementary: P_2 rises toward unity while $2P_1$ decreases toward zero as frequency grows. This reflects a gradual power transfer between the coupled branches across an avoided-crossing region. At low frequencies, the power

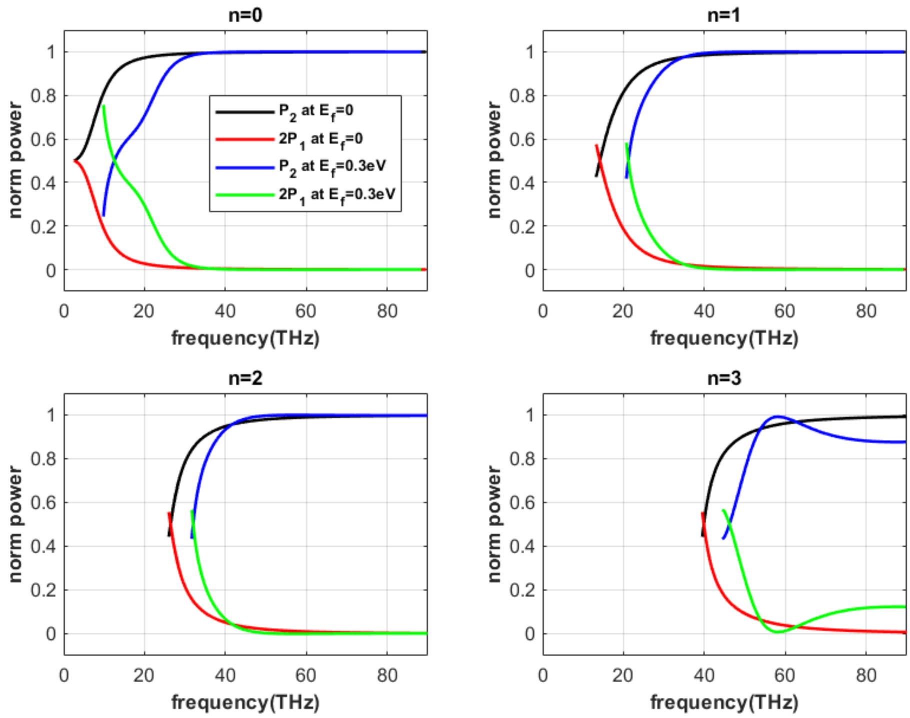

Figure 7: Normalized power carried by the outer claddings ($2P_1$) and the core layer (P_2) as a function of frequency for mode orders n =0, 1, 2, and 3 under all-dielectric conditions.

is shared almost equally ($\approx$ 50%) between the core and outer layers. As frequency increases, the energy concentrates into the mode associated with P_2. Raising E_F from 0 to 0.3 eV shifts this coupling region to lower frequencies and narrows the transition bandwidth due to the larger surface conductivity, which strengthens the plasmonic interaction with the guided modes. As the mode order increases, the conversion frequency shifts upward, and the curves present small kinks or discontinuities just before the transition. For the $n = 3$ mode, an incomplete power transfer is observed for the doped case: P_2 (blue) only recovers to about 0.9 and $2P_1$ (green) rises back to 0.1 at high frequencies, suggesting a secondary multi-resonant interaction with the graphene plasmons.

Lastly, Fig. 8 demonstrates the normalized power distribution when the central core layer is replaced by a negative-permeability metamaterial ($\mu_2 = -1.6$) for mode orders $n = 1$ to 4, where black/red represent $E_F = 0$ eV and blue/green represent $E_F = 0.3$ eV. The most striking difference from the conventional core case is that P_2 now evolves toward -1 instead of $+1$, while $2P_1$ still goes to zero from a positive value near $+0.5$. This sign inversion acts as a direct physical signature of the negative effective parameters of the metamaterial core. The power flux confined within the metamaterial layer becomes anti-parallel to the direction of phase propagation, meaning that the metamaterial supermode behaves as a backward-wave mode with a negative time-averaged Poynting vector. Conversely, the conventional outer layers still support forward propagation, keeping $2P_1$ positive at lower frequencies. As frequency increases, the system shifts from a balanced power-sharing state ($|P_2| \approx |2P_1| \approx 0.5$) toward complete power transfer where $|P_2| \to 1$ and $2P_1 \to 0$. Increasing E_F to 0.3 eV shifts the coupling frequency downward, confirming that the enhanced graphene conductivity accelerates the hybridization. For $n = 4$, both the intrinsic and doped curves exhibit a secondary dip/rise feature around 50–60 THz, proving the emergence of a secondary graphene-plasmon/metamaterial-mode coupling. This unique mixture of graphene tunability and metamaterial-induced backward waves can be exploited to design reconfigurable THz backward-wave couplers and direction-controllable mode converters.

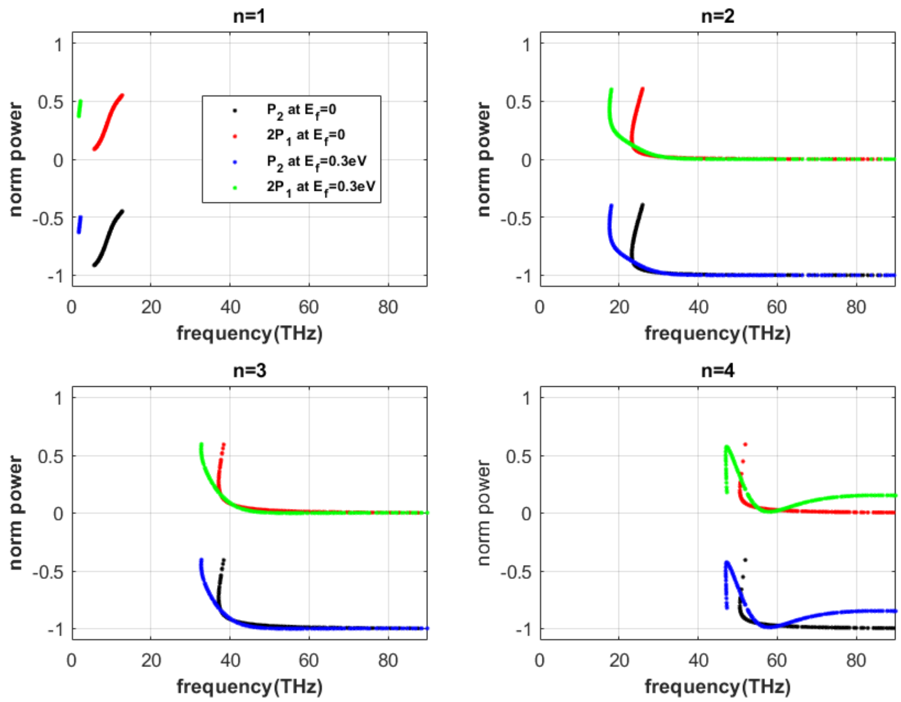

Figure 8: Power flow associated with the outer layers and the core layer demonstrating backward-wave propagation ($P_2 \to -1$) due to the metamaterial core ($\mu_2 = -1.6$).

6 Conclusions

The control of electromagnetic waves using three-layer-core slab waveguides with metamaterials and graphene as interfaces has the potential to be both versatile and effective. Derived dispersion relations and power flux expressions suggest the loss and gain of modal features with respect to confinement of electromagnetic fields to the direction of travel, which can be consistently modified via the graphene Fermi level and the metamaterial's effective magnetic permeability. For specific metamaterial designs, the TE_0 fundamental mode can be present or absent, while higher-order fundamental modes can be present over a broad spectrum of design parameters. Analyzed power flux reveals slow-wave and reverse-wave propagation resulting from combined forward and backward wave propagation. Post-fabrication control of the dispersion of the waveguide structure can be achieved via electrical control of graphene surface conductivity, revealing the tunability of these devices for electromagnetic and photonic applications. The results show that graphene–metamaterial slab waveguides have a high potential for use as flexible tunability platforms for next-generation electromagnetic and photonic devices.

[1] X. Wang, Y. Zhang, H. Liu, et al., *Graphene-Based Absorber: Tunable, Highly Sensitive, Six-Frequency*, Molecules, **30**(8), 1688 (2025).

[2] A. Ali, A. Mitra, and B. Aïssa, *Metamaterials and metasurfaces: A review from the perspectives of materials, mechanisms and advanced metadevices*, Nanomaterials, **12**(6), 1027 (2022).

[3] J. Krupka, *Materials with Negative Permittivity or Negative Permeability: Review, Electrodynamic Modelling, and Applications*, Materials **18**(2), 423 (2025).

[4] Y. Zhang, R. Feng, B. Shi, et al., *Ultra-Compact Reflective Waveguide Mode Converter Based on Slanted-Surface and Subwavelength Metamaterials*, Photonics, **11**(9), 838 (2024).

[5] Y. Lei, T. Zhang, Y. Lin, et al., *Graphene and Beyond: Recent Advances in Two-Dimensional Materials Synthesis, Properties, and Devices*, ACS Nanosci. Au **2**(6), 450 (2022).

[6] S. Qamar, N. Ramzan, and W. Aleem, *Graphene dispersion, functionalization techniques and applications: A review*, Synth. Met. **307**, 117697 (2024).

[7] L. Wang, N. An, X. He, et al., *Dynamic and active THz graphene metamaterial devices*, Nanomaterials **12**(12), 2097 (2022).

[8] M. Jablan, H. Buljan, and M. Soljačić, *Plasmonics in graphene at infrared frequencies*, Phys. Rev. B **80**, 245435 (2009).

[9] F. Razzaz, A. Nawaz, and A. Ghaffar, *Tunable properties of graphene-loaded waveguide surrounded by magnetic materials*, Dig. J. Nanomater. Bios. 2024, **19**(1), 283 (2024).

[10] M. Heidari and V. Ahmadi, *Design and analysis of a graphene magneto-plasmon waveguide for plasmonic mode switch*, IEEE Access **7**, 43406 (2019).

[11] F. M. Zhang, Y. He, and X. Chen, *Guided modes in graphene waveguides*, Appl. Phys. Lett. **94**, 212105 (2009).

[12] G. W. Hanson, *Dyadic Green's functions and guided surface waves for a surface conductivity model of graphene*, J. Appl. Phys. **103**, 064302 (2008).

[13] H. Salman and H. Yasser, *Design and Analysis of a Hybrid Plasmonic Waveguide with Chiral Metamaterial and Graphene Interfaces*, J. Microw. Optoelectron. Electromagn. Appl. **23**(04), e2024283713 (2024).

[14] H. Li, D. Zhang, and H. Zhu, *PTFE-based circular terahertz dielectric waveguides*, Photonics **11**(10), 921 (2024).

[15] Z. Ullah, I. Nawi, G. Witjaksono, et al., *Dynamic absorption enhancement and equivalent resonant circuit modeling of tunable graphene-metal hybrid antenna*, Sensors **20**(11), 3187 (2020).

[16] M. J. Maleki, M. Soroosh, and F. Haddadan, *Chapter 5: Graphene-Based Optical Waveguides for Surface Plasmon Polariton Transmission*, in: Optical Waveguide Technology and Applications, edited by K. Y. Kim, (IntechOpen, London, 2024).

[17] L. Pincherle, *Electromagnetic waves in metal tubes filled longitudinally with two dielectrics*, Phys. Rev. **66**, 11 (1944).

[18] S. V. Shchelkunov, T. C. Marshall, G. Sotnikov, et al., *Comparison of experimental tests and theory for a rectangular two-channel dielectric wakefield accelerator structure*, Phys. Rev. ST Accel. Beams **15**, 031301 (2012).

[19] S. Kumar, A. Kumari, and B. Pradhan, *Analysis of evanescent field of TE and TM mode in the grounded slab metamaterial waveguide structure*, Optik **126**(23), 3706 (2015).

[20] P. Markos and C. M. Soukoulis, *Wave Propagation: From Electrons to Photonic Crystals and Left-Handed Materials*, (Princeton University Press, Princeton, NJ, 2008).

[21] M. Baqir and P. Choudhury, *On the energy flux through a uniaxial chiral metamaterial made circular waveguide under PMC boundary*, J. Electromagn. Waves Appl. **26**(16), 2165 (2012).